Investigation of Li-ion transport in $Li_7P_3S_{11}$ and solid-state lithium batteries

Yu, Chuang; Ganapathy, Swapna; van Eck, Ernst R.H.; van Eijck, Lambert; de Klerk, Niek; Kelder, Erik M.; Wagemaker, Marnix

DOI
10.1016/j.jechem.2018.12.017

Publication date
2019

Document Version
Final published version

Published in
Journal of Energy Chemistry

Journal of Energy Chemistry 38 (2019) 1–7

Contents lists available at ScienceDirect

Journal of Energy Chemistry

journal homepage: www.elsevier.com/locate/jechem

http://www.journals.elsevier.com/journal-of-energy-chemistry/

Investigation of Li-ion transport in $Li_7P_3S_{11}$ and solid-state lithium batteries

Chuang Yu[a,*], Swapna Ganapathy[a], Ernst R. H. van Eck[b], Lambert van Eijck[a], Niek de Klerk[a], Erik M. Kelder[a], Marnix Wagemaker[a]

[a] Department of Radiation Science and Technology, Delft University of Technology, Mekelweg 15, 2629JB Delft, the Netherlands
[b] Institute for Molecules and Materials, Radboud University Nijmegen, Heyendaalseweg 135, 6525 AJ Nijmegen, the Netherlands

ARTICLE INFO

Article history:
Received 3 December 2018
Revised 21 December 2018
Accepted 24 December 2018
Available online 28 December 2018

Keywords:
$Li_7P_3S_{11}$
Li-ion transport
Spin-lattice NMR
Exchange NMR
Solid-state battery

ABSTRACT

The high Li-ion conductivity of the $Li_7P_3S_{11}$ sulfide-based solid electrolyte makes it a promising candidate for all-solid-state lithium batteries. The Li-ion transport over electrode-electrolyte and electrolyte-electrolyte interfaces, vital for the performance of solid-state batteries, is investigated by impedance spectroscopy and solid-state NMR experiments. An all-solid-state Li-ion battery is assembled with the $Li_7P_3S_{11}$ electrolyte, nano-Li_2S cathode and Li-In foil anode, showing a relatively large initial discharge capacity of 1139.5 mAh/g at a current density of 0.064 mA/cm^2 retaining 850.0 mAh/g after 30 cycles. Electrochemical impedance spectroscopy suggests that the decrease in capacity over cycling is due to the increased interfacial resistance between the electrode and the electrolyte. 1D exchange ^{7}Li NMR quantifies the interfacial Li-ion transport between the uncycled electrode and the electrolyte, resulting in a diffusion coefficient of $1.70(3)\times10^{-14}$ cm^2/s at 333 K and an energy barrier of 0.132 eV for the Li-ion transport between Li_2S cathode and $Li_7P_3S_{11}$ electrolyte. This indicates that the barrier for Li-ion transport over the electrode-electrolyte interface is small. However, the small diffusion coefficient for Li-ion diffusion between the Li_2S and the $Li_7P_3S_{11}$ suggests that these contact interfaces between electrode and electrolyte are relatively scarce, challenging the performance of these solid-state batteries.

1. Introduction

The increased interest in solid-state electrolytes for lithium batteries is primarily because of safety issues arising from the use of liquid organic electrolytes in conventional Li-ion batteries [1]. These flammable liquids can cause serious problems due to leakage and lead to gas evolution when operating at elevated temperatures and at higher voltages [2,3]. Unlike the liquid electrolyte, a solid electrolyte does not suffer from these drawbacks and in addition, improves the thermal and mechanical stability of the battery and is suggested to provide the possibility to work in a higher voltage window under extreme conditions [4]. However, solid electrolytes have their own bottlenecks, namely low Li-ion conductivity, interfacial contacts and harsh synthesis conditions including extremely elevated temperatures or air sensitivity. Therefore, exploring alternative synthesis route for old solid electrolytes in addition to the search for new solid electrolyte materials with high Li-ion conductivity is currently one of the key issues for the development of all-solid-state lithium batteries.

Various kinds of lithium ion conductors, such as Li_3PO_4-Li_4SiO_4 [5,6], the LISICON family $Li_{1+x}Ti_{2-x}M_x(PO_4)_3$ (M=Al, Sc, Y, La) [7], Li-β-alumina [8], perovskite-type $Li_{3x}La_{0.67-x}TiO_3$ [9], and garnet-related $Li_5La_3M_2O_{12}$ (M=Ta, Nb) [10] and its analogues $Li_7La_3Zr_2O_{12}$ [11] have been reported in literature. Most of these have a very low lithium conductivity falling in the range of 10^{-7}–10^{-4} S/cm at room temperature, which is far lower than that of currently used liquid organic electrolytes, which are of the order of 10^{-2} S/cm at 298 K. Fuminori et al. reported a glass ceramic with a composition of $Li_7P_3S_{11}$ precipitated from Li_2S-P_2S_5 glasses, showing ultrafast Li^+ ion conductivity of 10^{-3} S/cm at room temperature [12]. Further research revealed an enhancement of the ionic conductivity when this material was mixed with phases, such as LiX (X = Cl, Br, and I) [13,14], Li_2O [15], P_2O_5 [16,17], P_2S_3 [17,18] and Li_3PO_4 [19]. This solid electrolyte has successfully been combined with cathode materials like S [20–22]/Li_2S [23–25], $LiCoO_2$ [26], layered $LiMn_xNi_yCo_zO_2$ ($x+y+z=1$) [27], CuS [28], and Fe_2O_3 [29].

Of these cathode materials, Li_2S provides a high theoretical capacity (1170 mAh/g) and is easy to process for solid-state battery

* Corresponding author.
E-mail address: yuchuang1985@gmail.com (C. Yu).

https://doi.org/10.1016/j.jechem.2018.12.017

applications. As previously reported [30–32], the interfacial resistance between the cathode and the solid electrolyte is a significant impediment to solid-state cell performance. It must be minimized in order to achieve necessary electrochemical performance. However, there are not many methods available to detect the processes at the interphase between the cathode and the solid electrolyte. The most commonly used method is electrochemical impedance spectroscopy (EIS), which only provides a rough estimation of the interfacial resistance. Other methods like transmission electron microscopy (TEM) have been used to visualize the interfacial layer formed after charging the solid-state battery between the electrode and the solid electrolyte [33]. This method, however, provides only qualitative insight into the nature/composition of the interface, further highlighting the difficulty in probing interfacial Li^+ ion transport between the cathode and solid electrolyte.

Solid state NMR is a versatile method to study the structure and dynamics of materials used for both Li- and Na-ion batteries [34,35]. It can not only be used to investigate the structural changes occurring in the electrodes during the (dis)charge process [36] and the role of defects in the ionic conduction of electrode and electrolyte materials, but also to probe the correlation effects, timescales, activation energies and the ionic diffusion mechanism [37]. Recently, both one-dimensional (1D) and two-dimensional (2D) ^{7}Li-^{7}Li ion exchange NMR were successfully applied to study Li-ion transport from picoseconds to seconds for both the bulk argyrodite $Li_6PS_5Cl(Br)$ solid electrolyte and across the interface in a Li_2S-$Li_6PS_5Cl(Br)$ electrode-electrolyte cathodic mixtures, providing valuable insight into the effect of battery cycling on interfacial Li-ion transport [38,39].

In this work, a detailed understanding of the Li-ion dynamics in the $Li_7P_3S_{11}$ solid electrolyte is pursued by distinguishing local Li-ion mobility, bulk diffusion, and the impact of grain boundaries using AC impedance and temperature dependent ^{7}Li solid state NMR. Nano-Li_2S and Li-In foil were chosen as electrode materials and combined with the $Li_7P_3S_{11}$ solid electrolyte to assemble nano-Li_2S/$Li_7P_3S_{11}$/Li-In solid-state cells. The assembled cells showed excellent discharge capacities and cycling performance, retaining almost 850 mAh/g for 30 cycles. EIS measurements reveal that the interfacial resistance changes during the cycling. ^{7}Li-^{7}Li ion exchange NMR was performed to probe the Li-ion transport across the nano-Li_2S and $Li_7P_3S_{11}$ interface, providing new insights into the Li-ion transport restrictions, the origin of the internal resistance in the nano-Li_2S/$Li_7P_3S_{11}$/Li-In solid-state cells.

2. Experimental

Reagent-grade Li_2S (99.98%, Sigma-Aldrich) and P_2S_5 (99%, Sigma-Aldrich) crystalline powders were chosen as the raw materials. The mixture of the starting materials was filled into a Tungsten Carbide (WC) coated jar with 10 WC balls (8 g each) and then ball-milled with a planetary ball mill apparatus (Fritsch, Model Pulverisette 6) at a rotation speed of 400 rpm for 20 h. The ball-milling process was performed by milling for 5 min and then a rest time of 1 min. The amorphous 70Li_2S-30P_2S_5 formation process was monitored by taking some powder for a XRD measurement at specific intervals during the entire ball-milling process. The sulfur-based glass-ceramic material was synthesized by annealing the amorphous glass at 270 °C for 3 h. Since all the starting materials and the products are very sensitive to moisture and oxygen, the transfer procedures were carried out in an argon-filled glove box.

Powder X-ray diffraction (XRD) patterns were collected over a two-theta range of 10°–80° to identify the crystalline phases of the prepared materials using Cu K_α X-rays (1.5406 Å at 45 kV and 40 mA) on a X'Pert Pro X-ray diffractometer (PANalytical). To prevent reaction with moisture and oxygen, the powder materials were sealed in an airtight XRD sample holder in an Argon filled glove box. The refinement was performed using the Fullprof program [40].

Ionic conductivities of the ball-milled powder and the final $Li_7P_3S_{11}$ solid electrolyte were measured by pelletizing the powder to a 10 mm diameter. Stainless-steel disks were attached to both faces of the pellets. AC impedance measurements were performed using an Autolab (PGSTAT302N) in the frequency range of 0.1–1 MHz with an applied voltage of 0.05 V.

Solid-state NMR measurements were performed on a Chemagnetics 400 Infinity spectrometer ($B_0 = 9.4$ T), operating at a ^{7}Li resonance frequency of 155.506 MHz. The $\pi/2$ pulse length was determined to be 3.25 μs with an RF field strength of 32.75 kHz. Chemical shifts were referenced with respect to a 0.1 M LiCl solution. The air sensitive sample was sealed in a custom-made Teflon tube in an Argon filled glove box (H_2O, $O_2 < 0.3$ ppm). Variable temperature measurements were performed using a 5 mm static goniometer probe from 153 K to 453 K. T_1 relaxation times were determined at various temperatures using a saturation recovery experiment. For the Li_2S-$Li_7P_3S_{11}$ mixture, additional one-dimensional (1D) exchange experiments were performed at temperatures ranging from 218 K to 333 K. The pulse sequence used has been described in detail elsewhere with the appropriate phase cycle for cancellation of direct magnetization that may occur after T_1 relaxation [41,42]. Briefly the sequence consists of $\pi/2$, τ, π, τ, $-\pi/2$, t_{mix}, $+\pi/2$, acquisition. An echo time τ ranging from 50 μs to 500 ms was utilized so as to preserve the intensity of the narrow $Li_7P_3S_{11}$ resonance and filter out the broad Li_2S resonance, effectively functioning as a T_2 filter. These 1D exchange experiments were performed for a range of mixing times, t_{mix}, to follow the spontaneous equilibrium exchange of Li between the $Li_7P_3S_{11}$ and Li_2S phases.

Laboratory-scale solid-state Li-S batteries were fabricated in the following manner. For the cathode with Li_2S, commercial Li_2S was first milled with a rotation speed of 500 rpm for 4 h, and then milled with $Li_7P_3S_{11}$, super P and carbon nanofibers with a weight ratio of 4:4:1.5:0.5 using a rotation speed of 110 rpm for 1 h to obtain the final cathode mixture. Subsequently, a two-layer pellet ($d = 10$ mm), consisting of 12 mg of the nano-Li_2S mixture and 88 mg of the $Li_7P_3S_{11}$ electrolyte, was obtained by applying a pressure of 6 tons. After that, two pieces of lithium and Indium are first pressed to form a Li-In anode, and then attached to the pellet electrolyte. Finally, the complete pellet was pressed under 2 tons for 30 s. The nano-Li_2S/$Li_7P_3S_{11}$/Li-In solid-state cell was (dis)charged with a current density of 0.064 mA/cm^2 between 0.4 and 3.0 V vs. Li-In. The obtained capacity was normalized by the weight of the Li_2S in the cathode mixture. Electrochemical Impedance Spectrometry (EIS) measurements were performed with an Autolab PGSTAT302N before and after the charge/discharge process in the frequency range of 0.1 Hz and 1 MHz with an applied voltage of 0.05 V.

3. Results and discussion

To reveal the influence of milling on the 70Li_2S-30P_2S_5 solid electrolyte phase formation, the mixture of Li_2S and P_2S_5 having a ratio of 70/30 (mol%) was mechanically milled at 370 rpm for different milling durations and measured by XRD as shown in Fig. 1(a). Diffraction peaks can be indexed to the starting Li_2S and P_2S_5 phases in the mixture after ball-milling for 1 h. As the milling duration is increased to 3 h, the reflections attributed to the P_2S_5 phase gradually disappear, while the reflections indexed to Li_2S are still strong. Moreover, a halo pattern appears in the low 2θ range, indicating that an amorphous phase is formed. As the milling duration is increased to 5 h, the diffraction peaks due to Li_2S are still visible, but are clearly decreased in intensity. In addition, the intensity of the reflections due to crystalline phases

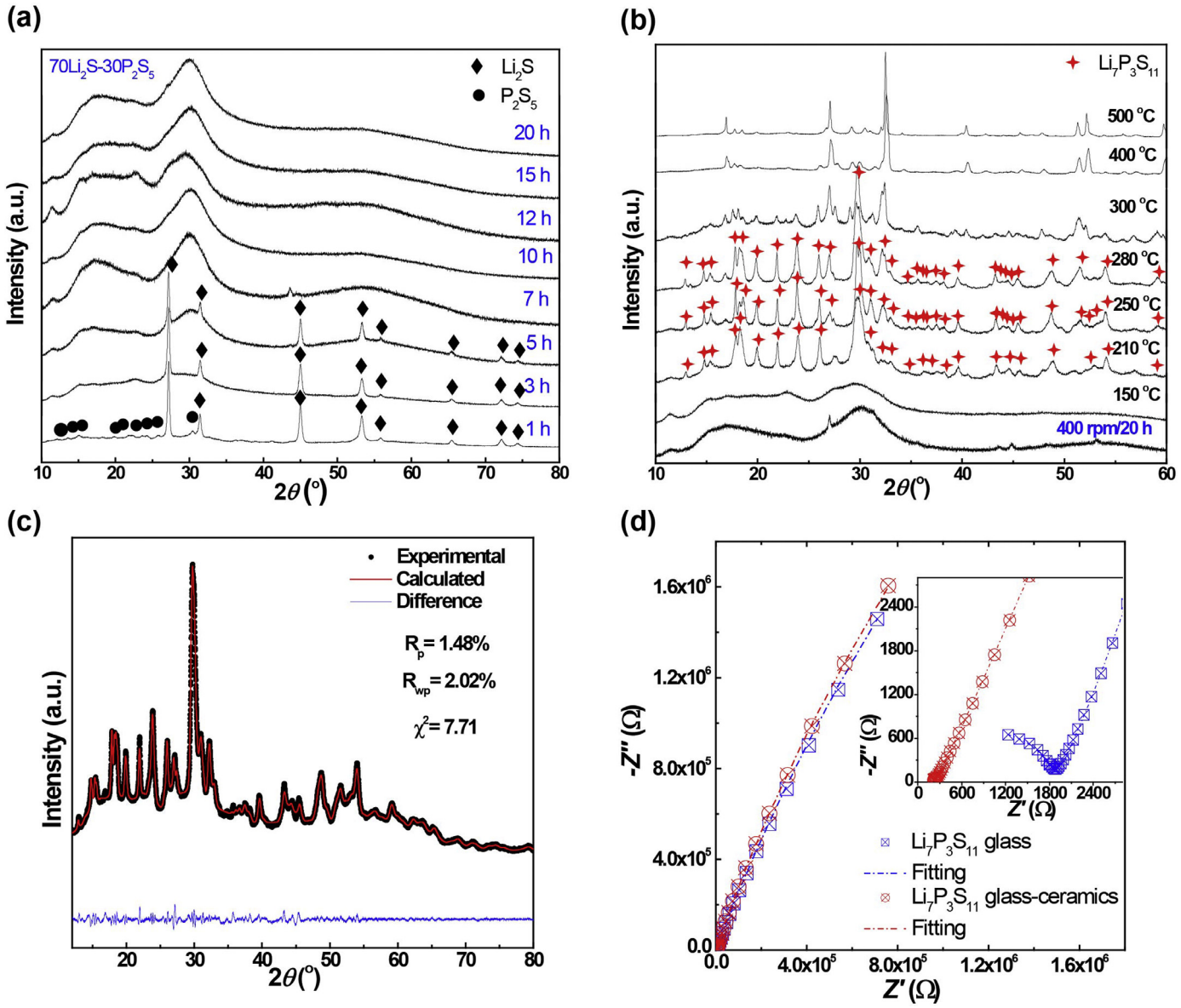

Fig. 1. (a) Powder XRD patterns of the prepared $70Li_2S$-$30P_2S_5$ glass after ball milling with a rotation speed of 400 rpm for different milling periods. (b) Powder XRD patterns of the $70Li_2S$-$30P_2S_5$ glass as a function of annealing temperature. The annealing duration is fixed at 3 h. (c) The XRD diffraction patterns of $Li_7P_3S_{11}$ obtained after annealing the ball milled powder (400 rpm for 20 h) at 270 °C for 3 h. Refinement was performed by the Rietveld method as implemented in Fullprof [43]. (d) Room temperature complex impedance plots of the $70Li_2S$-$30P_2S_5$ glass prepared by ball milling (400 rpm for 20 h) and heat treatment (270 °C/3 h).

gradually decreases with an increase of the ball-milling time. When the milling duration is longer than 7 h, the reflections due to Li_2S disappear. For milling durations in excess of 7 h, only a halo pattern is visible with no crystalline reflections indicating the formation of a completely amorphous phase. Previous reports showed that the $Li_7P_3S_{11}$ crystalline phase can be obtained by annealing the amorphous phase at a temperature higher than the crystallization temperatures (T_c) [12,44]. DSC was performed on the final ball-milled mixture to reveal the glass transition and crystallization process. The glass transition temperature is 204 °C and the crystallization temperature is 250 °C. The final amorphous phase powder was annealed at various temperatures for 3 h, the XRD of which is shown in Fig. 1(b). Annealing at 150 °C for 3 h produced no change in the diffraction pattern indicating that the amorphous phase is unaffected, in line with the glass transition temperature. The sample annealed at 210 °C, just above the glass transition temperature of 204 °C, shows the appearance of crystalline reflections in the diffraction pattern, a majority of which could be indexed to the $Li_7P_3S_{11}$ phase. After annealing at 250 °C, the reflections of the product are indexed to the pure $Li_7P_3S_{11}$ phase. This pure $Li_7P_3S_{11}$ phase persists at an annealing temperature of 280 °C, while some additional reflections due to the formation of unknown phases appear when the annealing temperature is increased to 300 °C, although the dominant phase still remains the $Li_7P_3S_{11}$ phase. At an annealing temperature of 400 °C and above a completely different phase is formed. Based on these XRD measurements, the pure $Li_7P_3S_{11}$ was found to form between 250 and 280 °C, and a final annealing temperature of 270 °C was selected. XRD refinement of the selected $Li_7P_3S_{11}$ is shown in Fig. 1(c), indicating that the annealed $Li_7P_3S_{11}$ is phase pure with an average particle size of 25 nm. Fig. 1(d) shows the complex impedance results of the sample before and after the annealing treatment. The sample after annealing at 270 °C shows a much smaller resistance than the ball-milled amorphous sample before annealing, delivering a Li-

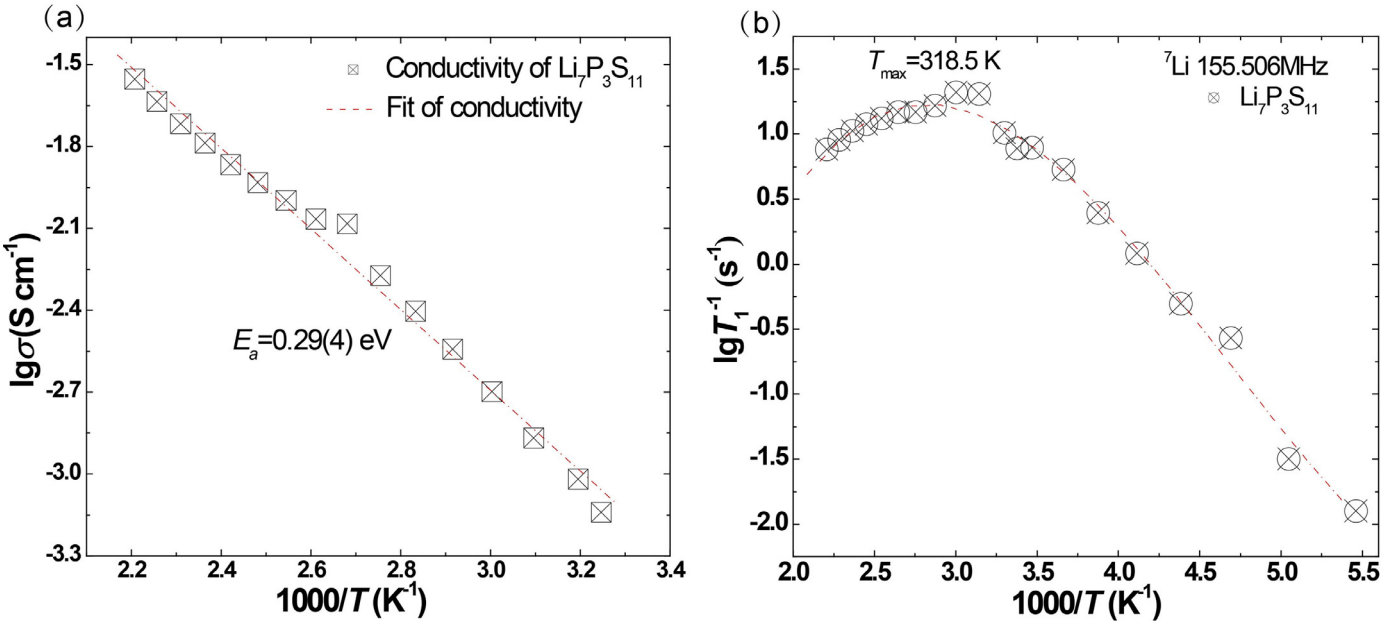

Fig. 2. Temperature-dependence of (a) the Li-ion conductivity resulting from impedance spectroscopy and (b) the ^{7}Li NMR spin-lattice relaxation rates $1/T_1$ in the laboratory frame for $Li_7P_3S_{11}$.

ion conductivity of $6.3(7)\times10^{-4}$ S/cm at 298 K, which is slightly smaller than values reported for this material in literature [12,45]. These results indicate that Li-ion conductivity of this sulfide-based LISICON-type conductor can be promoted by improving its crystallinity.

Fig. 2(a) shows the temperature dependence of the ionic conductivity of the $Li_7P_3S_{11}$ electrolyte from the impedance spectroscopy experiments. The ionic conductivity of $Li_7P_3S_{11}$ increases with increasing temperature reaching following an Arrhenius law. The activation energy (E_a) for the combined bulk and grain boundary contributions of $Li_7P_3S_{11}$ is calculated by fitting the total ionic conductivities with the Arrhenius equation resulting in 0.29(4) eV. This value is larger than the values reported by Mizuno et al. [12] and Seino et al. [44] obtained by impedance spectroscopy for crystalline $Li_7P_3S_{11}$ and densified $Li_7P_3S_{11}$, 18 kJ/mol (0.187 eV) and 26 kJ/mol (0.269 eV). The temperature dependent impedance data reflect the total lithium ion conductivity (σ_{Li}) and not the individual contributions of the bulk and grain-boundary conductivities. Measuring the NMR spin-lattice relaxation (SLR) rate allows to specifically measure the bulk conductivity σ_{Li} in fast ionic conductors [38,46]. Temperature-dependent ^{7}Li NMR SLR relaxation rates in the static laboratory frame (T_1) were measured at a Larmor frequency of 155.506 MHz, shown in Fig. 2(b). The asymmetric SLR rate peak, shown in Fig. 2(b), does not reflect the Bloembergen-Purcell-Pound (BPP) [47] symmetric peak (that should be expected for 3D uncorrelated motion) similar to what was reported by Wohlmuth et al. [48]. The low-temperature flank (the right side), where $\tau\cdot\omega_0 \gg 1$, the short range Li-diffusion dominates the $1/T_1$ relaxation, which follows an Arrhenius behavior, yielding an activation energy of 0.11(6) eV for this Li-diffusion process.

This value is significantly smaller than the values reported by Wohlmuth et al. [48] detected by both ^{7}Li and ^{6}Li SLR NMR at 116.6 MHz, which resulted in activation energies from 0.19 to 0.22 eV. The high-temperature flank (the left side) typically represents long range Li-ion diffusion, indicating an activation energy of 0.04(2) eV, which is also smaller than the 0.06 eV reported previously [48]. However, as concluded by Wohlmuth et al. [48], it is unlikely that this extremely small activation energy derived from the high-temperature flank is representing a realistic value for bulk diffusion; rather it reflects the disordered nature of the diffusional process leading to a distribution in hopping timescales [48]. Wohlmuth et al. [48] suggested at least three different relaxation rates for $Li_7P_3S_{11}$ glass ceramic by ^{6,7}Li NMR spin-lattice relaxation, and SLR rates measured in the rotating frame resulted in activations energies in the range of 0.22–0.26 eV. Therefore, the SLR rate measured at present can only be used to determine the Li-ion jump rate from the maximum jump rate at 318.5 K through the condition $\tau\cdot\omega_0\approx1$, where τ is the jump rate for lithium ion and ω_0 is associated with the frequency applied for the SLR NMR [49]. Based on the Larmor frequency (155.506 MHz) this results in a Li-ion jump rate of 9.77×10^{-8} s^{-1} in the bulk of crystalline $Li_7P_3S_{11}$ at 318.5 K, assuming a mean Li jump distance in $Li_7P_3S_{11}$ of 2.5 Å; this results in a self-diffusion coefficient of $1.02(0)\times10^{-7}$ cm^2/s at 318.5 K based on the Einstein–Smoluchowski equation [50] and a bulk conductivity of 0.0089(3) S/cm, on order of magnitude larger than the total ionic conductivity measured by impedance at 313 K, 0.0009(6) S/cm. This may indicate that electrolyte-electrolyte grain boundaries may lower the total conductivity as measured by impedance.

Fig. 3(a) shows the (dis)charge curves for the all-solid-state Li-S battery using the prepared $Li_7P_3S_{11}$ as solid electrolyte in combination with a Li_2S cathode and a Li-In foil anode. The solid-state cell shows an extremely low initial charge capacity and a high discharge capacity of 1139.5 mAh/g (calculated based on the weight of Li_2S in the cathode mixture) at a current density of 0.064 mA/cm^2 between 0.4 and 3.0 V vs. Li-In, which is almost 97.3% of its theoretical capacity (1170 mAh/g). The initial discharge capacity based on the total weight of Li_2S and $Li_7P_3S_{11}$ is 569.8 mAh/g. It should be noted that the initial charge capacity is less than 400 mAh/g, much lower than the initial discharge capacity, suggesting that a large number of lithium ions are extracted from the Li-In anode. The extremely high discharge capacities obtained in the subsequent cycles may come from the extra Li extracted from the Li-In anode side. However, the mechanism why lithium extraction was impeded from the cathode mixture during the initial process is unclear. After the first cycle, the cell shows a relatively high (dis)charge capacity and good cycling performance at room temperature. After 30 cycles, the discharge capacity is still exceeding

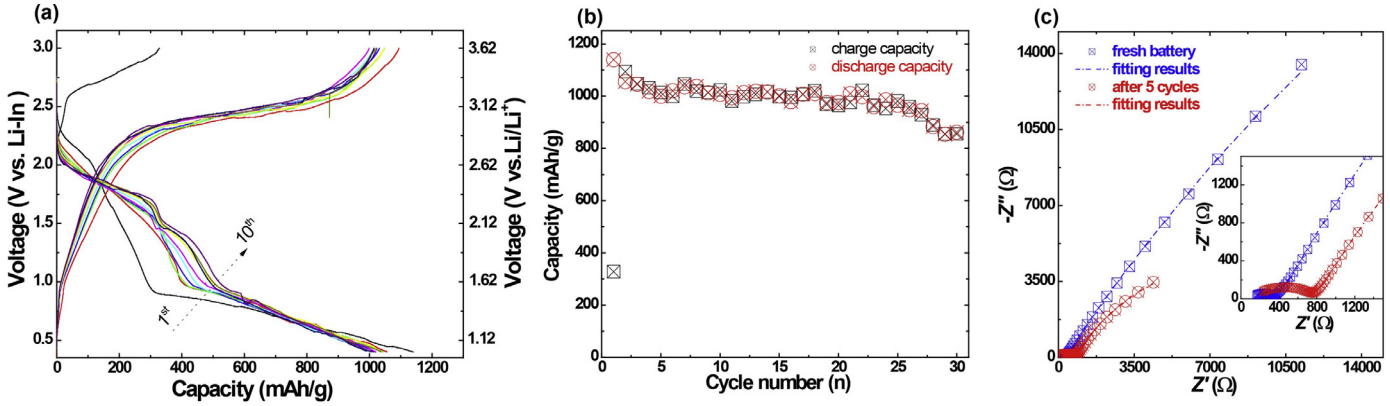

Fig. 3. The charge/discharge plots (a) and cycling performance (b) of the solid-state Li-S cell using nano-Li_2S as the active material. The charge/discharge current density was set at 0.064 mA/cm^2 (5.03×10^{-5} A), and the lower and upper voltage cut-off were set to 0.4 and 3.0 V vs. Li-In. (c) Electrochemical impedance spectroscopy (EIS) of the fresh and after 5 cycles nano-Li_2S/$Li_7P_3S_{11}$/Li-In solid-state batteries. The square and circle symbols represent the impedance of the fresh and 5 cycles solid-state batteries, respectively, and the blue and red dashed lines represent fits using an equivalent circuit $R_1(R_2Q_2)(R_3Q_3)$.

850.0 mAh/g, which was calculated based on the weight of Li_2S in the cathode mixture, indicating relatively good cycling performance for this type of solid-state cells, as shown in Fig. 3(b). This is most likely the result of the high Li-ion mobility of the prepared $Li_7P_3S_{11}$ in combination with the low charge/discharge current density, and the small nano-size (38 nm) of the Li_2S cathode, all contributing to a low internal resistance. Potentially, also the electronic wiring achieved by a combination of spherical super P and nano-carbon fiber wires contributes to the relatively good performance. The $Li_7P_3S_{11}$ solid electrolyte decomposition in the cathode mixture may also contribute to the capacity during (dis)charging. To clarify this, an all-solid-state battery using $Li_7P_3S_{11}$–C as the cathode mixture, $Li_7P_3S_{11}$ as the solid electrolyte and In as the anode material was assembled, as shown in SI Fig. 1. The reason we chose In as the anode material instead of Li-In due to that we want to make sure that lithium ions can only come from $Li_7P_3S_{11}$ in the cathode mixture during cycling. The $Li_7P_3S_{11}$–C/$Li_7P_3S_{11}$/In all-solid-state battery shows an initial charge capacity of 416.81 mAh/g and discharge capacity of 286.68 mAh/g with an initial coulombic efficiency of 68.78% at a cycling current density of 0.064 mA/cm^2. This indicates that at least 25.16% of the (dis)charge capacity during the first cycles in Fig. 2 is due to capacity related to the solid electrolyte material through oxidation and reduction reactions. After the initial cycle, the discharge capacities of the subsequent cycles maintain close to 250 mAh/g, suggesting that $Li_7P_3S_{11}$ in the cathode mixture can provide capacity for S-C-$Li_7P_3S_{11}$/$Li_7P_3S_{11}$/Li-In all-solid-state battery. The (dis)charge voltage profile observed for the nano-Li_2S/$Li_7P_3S_{11}$/Li-In solid-state cell is quite different compared to that reported elsewhere [24,25]. As shown in Fig. 3(a), the initial discharge curve shows two discharge plateaus, one located at a voltage higher than 2.0 V vs. Li-In, which may be associated with the decomposition of $Li_7P_3S_{11}$ in the cathode mixture, while the other plateau located at 0.9 V vs. Li-In is attributed to the electrochemical reaction of S cathode. In the subsequent cycles, only one charge plateau located at 2.3 V vs. Li-In is observed and three discharge plateaus located at 1.8, 1.4, and 0.9 V vs. Li-In are observed. Interestingly, it shows similar discharge plateaus as that of lithium ion batteries employing a Li_2S cathode. For the Li/S batteries with organic liquid electrolyte [51], where the 2.1–2.4 V region is associated with the formation of soluble polysulfides and the 1.5–2.1 V is associated with the reduction of soluble polysulfides to form the solid-state Li_2S. It is believed that the higher voltage plateau located at $\sim$ 1.8 V vs. Li-In is due to the reaction of Li_2S, which is attributed to the decomposition reaction of $Li_7P_3S_{11}$ during the initial cycle. Similar behavior has been already reported in other sulfide electrolytes, such as Li_6PS_5X (X = Cl, Br) in our recent research which is ongoing. The lower plateau located at 0.9 V vs. Li-In is the typical discharge plateau for an all-solid-state Li-S battery due to S active material. It should be mentioned that a new discharge plateau located at $\sim$ 1.4 V vs. Li-In appears after 5 cycles, which may be associated to other side product due to the decomposition of $Li_7P_3S_{11}$ in the cathode mixture. Additionally, EIS (electrochemical impedance spectroscopy) was applied to study the Li-ion dynamics in the nano-Li_2S/$Li_7P_3S_{11}$/Li-In solid-state cell. Fig. 3(c) shows the typical Nyquist plots of the fresh and cycled (after 5 cycles) solid-state cell. Two intersection points with the horizontal axis in the high (left side) and low (right side) frequencies are observed in the Nyquist plots, which are named R_1 and R_2. R_1 reflects the resistance of $Li_7P_3S_{11}$ electrolyte, and R_2-R_1 reflects the resistance of the Li_2S cathode-$Li_7P_3S_{11}$ electrolyte interface [19]. The resistance for $Li_7P_3S_{11}$ electrolyte and the interfacial part of the fresh cell are 113.0 and 146.6 Ω, while those for the battery after 5 cycles are 100.2 and 604.4 Ω. The resistance of Li_2S-$Li_7P_3S_{11}$ interface drastically increases during the first 5 cycles, which may be attributed to the formation of insulating side products at the interface during the first few cycles. Therefore, the Li-ion transport dynamics between the Li_2S cathode and $Li_7P_3S_{11}$ electrolyte will increasingly contribute to the internal resistance, limiting the electrochemical performance of the nano-Li_2S/$Li_7P_3S_{11}$/Li-In solid-state cell.

In previous work [38,39], it was shown that exchange NMR experiments can be used to unambiguously characterize Li-ion transport over the electrode-solid electrolyte interface, giving quantitative insight into the impact of the interface and interphases on Li-ion charge transport in all-solid-state batteries. At present, 1D NMR ^{7}Li exchange experiments between the fresh, uncycled, nano-Li_2S cathode material and the $Li_7P_3S_{11}$ solid electrolyte were performed at various temperatures. The resulting decrease in ^{7}Li signal of the $Li_7P_3S_{11}$ phase due to the Li-ion diffusion between Li_2S and $Li_7P_3S_{11}$ with increasing mixing time t_{mix} is shown in Fig. 4(a). To quantify the exchange between the two materials, the decaying $Li_7P_3S_{11}$ signal due to the magnetization transfer carried by the Li-ions is fitted with a diffusion model. The details about the model and data processing were provided in previous work [38,39]. To determine the diffusion coefficient from the exchange experiments requires the value of the average diffusion length d. For simplicity it is assumed that the diffusion distance starts from the center of a $Li_7P_3S_{11}$ particle to the center of a Li_2S particle and that shape of the particles of these two materials is spherical. This assumption most likely overestimates the diffusion distance, and hence the diffusion coefficient, because of the poor conductivity of Li_2S.

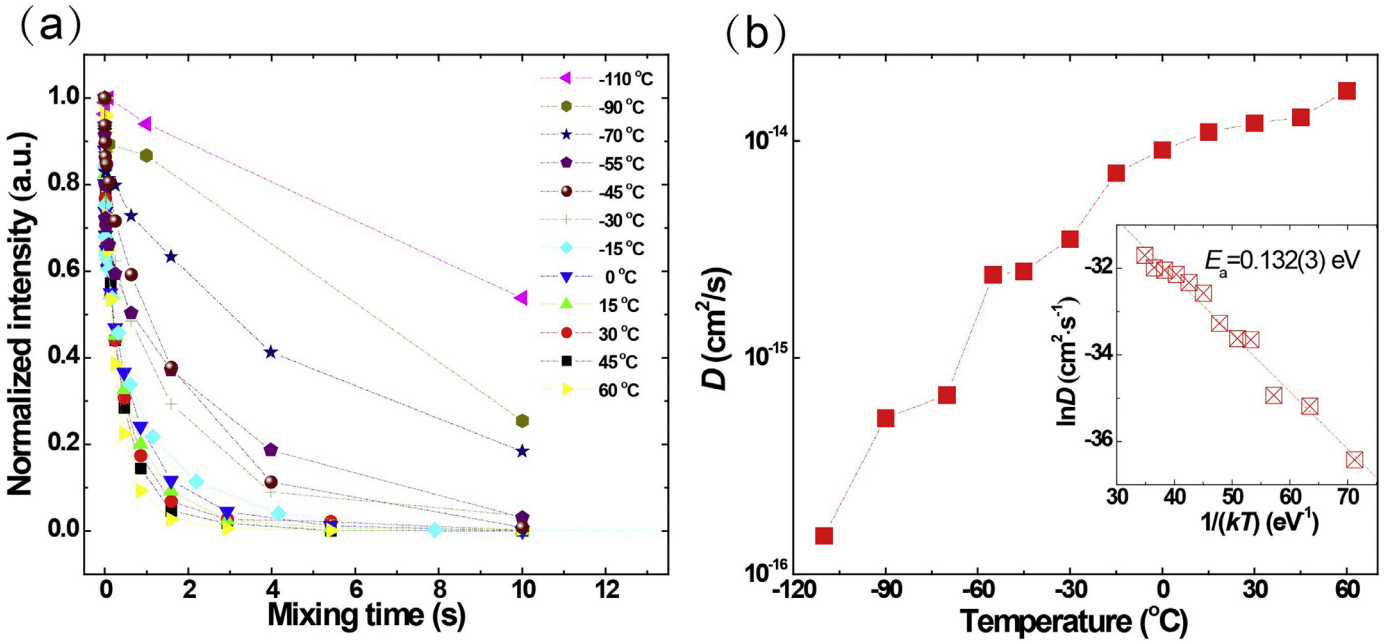

Fig. 4. (a) Normalized intensity of the static $Li_7P_3S_{11}$ ^7Li NMR spectrum, T_1 corrected, as a function of mixing time at different temperatures. (b) The Arrhenius plot of the diffusion rates at various temperatures. An Arrhenius law is used to fit the activation energy, E_a, representing the diffusion process over the boundary between the $Li_7P_3S_{11}$ solid electrolyte and the Li_2S phases.

This results in diffusion coefficients for Li_2S-$Li_7P_3S_{11}$ exchange of $2.41(7)\times10^{-15}$ cm^2/s at 218 K, $1.20(8)\times10^{-14}$ cm^2/s at 303 K, and $1.70(3)\times10^{-14}$ cm^2/s at 333 K, respectively. These values are many orders of magnitude smaller than the bulk diffusion coefficient for $Li_7P_3S_{11}$ amounting $1.02(0)\times10^{-7}$ cm^2/s at 318.5 K deduced by SLR NMR. The diffusion coefficient follows an Arrhenius behavior, shown in Fig. 4(b), yielding an activation energy of 0.132 eV. This relatively small activation energy E_a for the Li-ion exchange between Li_2S and $Li_7P_3S_{11}$ is much smaller than the activation energy of $Li_7P_3S_{11}$ deduced from the temperature dependent ionic conductivity (0.132 eV vs. 0.294 eV). This may indicate that mainly Li-ion transport near the Li_2S-$Li_7P_3S_{11}$ interfaces is measured by exchange NMR and that this transport is relatively facile compared to that in the $Li_7P_3S_{11}$ solid electrolyte material. The relatively small diffusion coefficient compared to the bulk conductivity suggests that there is very little Li_2S-$Li_7P_3S_{11}$ interface present that allows Li-ion transport. Therefore, establishing good wetting, resulting in abundant Li_2S-$Li_7P_3S_{11}$ interfaces, appears to be the key limitations of these solid-state batteries. In particular, the interface decomposition reactions and volumetric changes of the electrode materials will further challenge these interfaces.

4. Conclusions

The excellent solid electrolyte for solid-state Li-ion batteries, $Li_7P_3S_{11}$, with a high Li-ion conductivity of $6.3(7)\times10^{-4}$ S/cm at 298 K, was obtained by milling at 400 rpm for 20 h followed by annealing at 270 °C for 3 h. Temperature-dependent impedance and SLR NMR results show that the grain boundary resistance is the major hurdle for the improvement of ionic conductivity. $Li_7P_3S_{11}$ was applied to assemble solid-state Li-ion batteries of the configuration nano-Li_2S/$Li_7P_3S_{11}$/Li-In and delivers a discharge capacity of 1139.5 mAh/g for the initial cycle, retaining 850.0 mAh/g after 30 cycles. EIS shows that the decreasing of capacity is due to the increase of the interfacial resistance between Li_2S and $Li_7P_3S_{11}$. With 1D ^7Li NMR exchange experiments the diffusion coefficient is determined for diffusion between Li_2S and $Li_7P_3S_{11}$, and is found to be orders of magnitude smaller than the bulk diffusion coefficient for $Li_7P_3S_{11}$, indicating that establishing abundant interfaces that facilitate easy Li transport over the Li_2S-$Li_7P_3S_{11}$ interface are essential for solid-state battery performance.

Acknowledgments

The research leading to these results has received funding from the European Research Council under the European Union's Seventh Framework Programme (FP/2007-2013) / ERC Grant Agreement no. [307161] of M.W. Support from the Dutch organization of scientific research (NWO) for the solid-state NMR facility for advanced materials science in Nijmegen is gratefully acknowledged. The technical assistance of Hans Janssen, Gerrit Janssen and Jan Schoonbrood is gratefully acknowledged. The solid-state NMR facility for advanced material science at the Radboud University is greatly acknowledged for supporting this research. The assistance of Frans Ooms, Michel Steenvoorden and Kees Goubitz is gratefully acknowledged.

Supplementary materials

Supplementary material associated with this article can be found, in the online version, at doi:10.1016/j.jechem.2018.12.017.

References

[1] E. Quartarone, P. Mustarelli, Chem. Soc. Rev. 40 (2011) 2525–2540.
[2] M. Hu, X. Pang, Z. Zhou, J. Power Sources 237 (2013) 229–242.
[3] C.L. Campion, W. Li, B.L. Lucht, J. Electrochem. Soc. 152 (2005) A2327–A2334.
[4] E.P. Roth, C.J. Orendorff, Electrochem. Soc. Interface 21 (2012) 45–49.
[5] L. Zhang, L. Cheng, J. Cabana, G. Chen, M.M. Doeff, T.J. Richardson, Solid State Ionics 231 (2013) 109–115.
[6] Y. Deng, C. Eames, J.-N.l. Chotard, F. Laleře, V. Seznec, S. Emge, O. Pecher, C.P. Grey, C. Masquelier, M.S. Islam, J. Am. Chem. Soc. 137 (2015) 9136–9145.
[7] K. Arbi, M. Hoelzel, A. Kuhn, F. García-Alvarado, J. Sanz, Inorg. Chem. 52 (2013) 9290–9296.
[8] G. Farrington, W. Roth, Li+ conduction in the beta alumina structure, Superionic Conductors, Springer, 1976, pp. 418–419.
[9] S. Stramare, V. Thangadurai, W. Weppner, Chem. Mater. 15 (2003) 3974–3990.
[10] V. Thangadurai, J. Schwenzel, W. Weppner, Ionics 11 (2005) 11–23.
[11] R. Murugan, V. Thangadurai, W. Weppner, Angew. Chem. Int. Ed. 46 (2007) 7778–7781.

[12] F. Mizuno, A. Hayashi, K. Tadanaga, M. Tatsumisago, Adv. Mater. 17 (2005) 918–921.
[13] S. Ujiie, T. Inagaki, A. Hayashi, M. Tatsumisago, Solid State Ionics 263 (2014) 57–61.
[14] S. Ujiie, A. Hayashi, M. Tatsumisago, Solid State Ionics 211 (2012) 42–45.
[15] T. Ohtomo, A. Hayashi, M. Tatsumisago, K. Kawamoto, J. Non-Crystal. Solids 364 (2013) 57–61.
[16] K. Minami, F. Mizuno, A. Hayashi, M. Tatsumisago, J. Non-Crystal. Solids 354 (2008) 370–373.
[17] K. Minami, A. Hayashi, S. Ujiie, M. Tatsumisago, Solid State Ionics 192 (2011) 122–125.
[18] K. Minami, A. Hayashi, S. Ujiie, M. Tatsumisago, J. Power Sources 189 (2009) 651–654.
[19] B. Huang, X. Yao, Z. Huang, Y. Guan, Y. Jin, X. Xu, J. Power Sources 284 (2015) 206–211.
[20] M. Nagao, A. Hayashi, M. Tatsumisago, Electrochim. Acta 56 (2011) 6055–6059.
[21] T. Kobayashi, Y. Imade, D. Shishihara, K. Homma, M. Nagao, R. Watanabe, T. Yokoi, A. Yamada, R. Kanno, T. Tatsumi, J. Power Sources 182 (2008) 621–625.
[22] M. Nagao, Y. Imade, H. Narisawa, T. Kobayashi, R. Watanabe, T. Yokoi, T. Tatsumi, R. Kanno, J. Power Sources 222 (2013) 237–242.
[23] T. Takeuchi, H. Kageyama, K. Nakanishi, T. Ohta, A. Sakuda, T. Sakai, H. Kobayashi, H. Sakaebe, K. Tatsumi, Z. Ogumi, Solid State Ionics 262 (2014) 138–142.
[24] M. Nagao, A. Hayashi, M. Tatsumisago, J. Mater. Chem. 22 (2012) 10015–10020.
[25] M. Nagao, A. Hayashi, M. Tatsumisago, T. Ichinose, T. Ozaki, Y. Togawa, S. Mori, J. Power Sources 274 (2015) 471–476.
[26] F. Mizuno, A. Hayashi, K. Tadanaga, T. Minami, M. Tatsumisago, Solid State Ionics 175 (2004) 699–702.
[27] N. Machida, J. Kashiwagi, M. Naito, T. Shigematsu, Solid State Ionics 225 (2012) 354–358.
[28] A. Hayashi, T. Ohtomo, F. Mizuno, K. Tadanaga, M. Tatsumisago, Electrochem. Commun. 5 (2003) 701–705.
[29] H. Kitaura, K. Takahashi, F. Mizuno, A. Hayashi, K. Tadanaga, M. Tatsumisago, J. Electrochem. Soc. 154 (2007) A725–A729.
[30] N. Ohta, K. Takada, I. Sakaguchi, L. Zhang, R. Ma, K. Fukuda, M. Osada, T. Sasaki, Electrochem. Commun. 9 (2007) 1486–1490.
[31] K. Takada, Langmuir 29 (2013) 7538–7541.
[32] C. Yu, L. van Eijck, S. Ganapathy, M. Wagemaker, Electrochim. Acta 215 (2016) 93–99.
[33] A. Sakuda, A. Hayashi, M. Tatsumisago, Chem. Mater. 22 (2009) 949–956.
[34] C.P. Grey, N. Dupré, Chem. Rev. 104 (2004) 4493–4512.
[35] A. Kuhn, M. Kunze, P. Sreeraj, H.-D. Wiemhöfer, V. Thangadurai, M. Wilkening, P. Heitjans, Solid State Nuclear Magn. Reson. 42 (2012) 2–8.
[36] F.d.r. Blanc, M. Leskes, C.P. Grey, Acc. Chem. Res. 46 (2013) 1952–1963.
[37] M. Wilkening, P. Heitjans, ChemPhysChem 13 (2012) 53–65.
[38] C. Yu, S. Ganapathy, N.J. de Klerk, I. Roslon, E.R. Van Eck, A.P. Kentgens, M. Wagemaker, J. Am. Chem. Soc. 138 (2016) 11192–11201.
[39] C. Yu, S. Ganapathy, E.R. Van Eck, H. Wang, S. Basak, Z. Li, M. Wagemaker, Nat. Commun. 8 (2017) 1086.
[40] J. Rodriguez-Carvajal, in: Proceedings of the Satellite Meeting on Powder Diffraction of the XV Congress of the IUCr, Toulouse, France:[sn], 1990.
[41] M. Wagemaker, A. Kentgens, F. Mulder, Nature 418 (2002) 397–399.
[42] S. Ganapathy, E.R.H. van Eck, A.P.M. Kentgens, F.M. Mulder, M. Wagemaker, Chem. A Eur. J. 17 (2011) 14811–14816.
[43] J. Rodriguez-Carvajal, Physica B 55 (1993) 192.
[44] Y. Seino, T. Ota, K. Takada, A. Hayashi, M. Tatsumisago, Energy Environ. Sci. 7 (2014) 627–631.
[45] K. Minami, F. Mizuno, A. Hayashi, M. Tatsumisago, Solid State Ionics 178 (2007) 837–841.
[46] K. Volgmann, V. Epp, J. Langer, B. Stanje, J. Heine, S. Nakhal, M. Lerch, M. Wilkening, P. Heitjans, Zeitschr. Physik. Chem. 231 (2017) 1215–1241.
[47] N. Bloembergen, E.M. Purcell, R.V. Pound, Phys. Rev. 73 (1948) 679.
[48] D. Wohlmuth, V. Epp, M. Wilkening, ChemPhysChem 16 (2015) 2582–2593.
[49] A. Kuhn, J.-Y. Choi, L. Robben, F. Tietz, M. Wilkening, P. Heitjans, Zeitschr. Physik. Chem. 226 (2012) 525–537.
[50] H. Mehrer, Diffusion in Solids: Fundamentals, Methods, Materials, Diffusion–Controlled Processes, Springer Science & Business Media, 2007.
[51] S.-E. Cheon, K.-S. Ko, J.-H. Cho, S.-W. Kim, E.-Y. Chin, H.-T. Kim, J. Electrochem. Soc. 150 (2003) A796–A799.